tion of positive and negative spatiotemporal feedback that is able to accurately direct wave propagation.

The control methods presented here also represent potential tools for investigating spatiotemporal dynamical systems. Our study has demonstrated that there is a direct proportionality between wave trajectory curvature and the excitability gradient for a given wave size (*24*). Control methods also provide a means for probing underlying mechanisms, as demonstrated in studies of homogeneous chemical systems (*25*, *26*). Such techniques are closely related to the relaxation methods developed by Eigen and co-workers (*27*) for probing chemical kinetics. Spatiotemporal behavior is pervasive in living systems, and control methods offer a promising direction for probing their underlying mechanisms.

References and Notes

1. M. Kim *et al.*, *Science* **292**, 1357 (2001).
2. J. Wolff, A. G. Papathanasiou, I. G. Kevrekidis, H. H. Rotermund, G. Ertl, *Science* **294**, 134 (2001).
3. V. Petrov, Q. Ouyang, H. L. Swinney, *Nature* **388**, 655 (1997).
4. A. L. Lin *et al.*, *Phys. Rev. E* **62**, 3790 (2000).
5. V. K. Vanag, L. Yang, M. Dolnik, A. M. Zhabotinsky, I. R. Epstein, *Nature* **406**, 389 (2000).
6. O. Steinbock, V. S. Zykov, S. C. Müller, *Nature* **366**, 322 (1993).
7. S. Grill, V. S. Zykov, S. C. Müller, *Phys. Rev. Lett.* **75**, 3368 (1995).
8. A. N. Zaikin, A. M. Zhabotinsky, *Nature* **225**, 535 (1970).
9. B. J. Gluckman, H. Nguyen, S. L. Weinstein, S. J. Schiff, *J. Neurosci.* **21**, 590 (2001).
10. L. Kuhnert, *Nature* **319**, 393 (1986).
11. E. Mihaliuk, T. Sakurai, F. Chirila, K. Showalter, *Faraday Discuss. Chem. Soc.* **120**, 383 (2002).
12. A fresh silica gel medium was prepared before each experiment by acidifying an aqueous solution of 10% (w/w) Na_2SiO_3 and 1.0×10^{-3} M $Ru(bpy)_3{}^{2+}$ with H_2SO_4. The gel was bathed in a catalyst-free BZ solution of 0.28 M $NaBrO_3$, 0.05 M malonic acid, 0.165 M bromomalonic acid, and 0.36 M H_2SO_4. The reaction mixture residence time and temperature were 4.5×10^2 s and 15.0°C. The spatial resolution of the camera and projector, each with an eight-bit gray level range, was 0.07 mm, and the time step for applying a new illumination pattern calculated from Eq. 1 was 2.0 s. The light at $\lambda = 460$ nm with a bandwidth $\Delta\lambda = 10$ nm had a maximum intensity ϕ, measured at the gel, of 0.5 mW/cm². Video camera measurements of gray levels $p(x, y)$ were obtained by interrupting the control algorithm for 0.1 s and applying a uniform illumination. The coordinates for the "center of mass" of a wave were calculated according to:
$$x_{cm} = \left[\sum_{x=1,y=1}^{n_x,n_y} (x\Theta[p(x,y) - p_{th}])\right]/A$$
$$y_{cm} = \left[\sum_{x=1,y=1}^{n_x,n_y} (y\Theta[p(x,y) - p_{th}])\right]/A$$
where x and y are spatial variables, n_x and n_y define the maximum size of the medium, $p(x, y)$ is the gray level, Θ is the Heaviside function giving 0 or 1 in the summations, and A is the wave area defined in Eq. 1.
13. Z. Noszticzius, W. Horsthemke, W. D. McCormick, H. L. Swinney, W. Y. Tam, *Nature* **329**, 619 (1987).
14. S. Kádár, T. Amemiya, K. Showalter, *J. Phys. Chem. A* **101**, 8200 (1997).
15. V. K. Vanag, A. M. Zhabotinsky, I. R. Epstein, *J. Phys. Chem. A* **104**, 8207 (2000).
16. I. Sendiña-Nadal, E. Mihaliuk, J. Wang, V. Pérez-Muñuzuri, K. Showalter, *Phys. Rev. Lett.* **86**, 1646 (2001).
17. R. H. Hooverman, *J. Appl. Phys.* **34**, 3505 (1963).
18. Numerical studies were carried out using an Oregonator model of the photosensitive BZ reaction (*19*–*21*): $[(\partial u)/(\partial t)] = D_u\nabla^2 u + [1/(\varepsilon)](u - u^2 - (\phi + fv)[(u - q)/(u + q)])$, $[(\partial v)/(\partial t)] = u - v$, where u and v are the concentrations of $HBrO_2$ and $Ru(bpy)_3{}^{3+}$, and ϕ is the rate of photochemical production of Br^-. All simulations were carried out using the Crank-Nicholson method with parameters $f = 2.5$, $q = 0.0002$, $\varepsilon = 0.01$, $D_u = 0.1$, the time step $dt = 0.001$, and the spatial grid $dx = 0.02$. Control of wave motion was carried out using Eq. 1 analogous to the experimental study, except that the wave area was determined by counting pixels with the variable u above a threshold value u_{th}.
19. R. J. Field, R. M. Noyes, *J. Chem. Phys.* **60**, 1877 (1974).
20. J. J. Tyson, P. C. Fife, *J. Chem. Phys.* **73**, 2224 (1980).
21. H. J. Krug, L. Pohlmann, L. Kuhnert, *J. Chem. Phys.* **94**, 4862 (1990).
22. G. Li, Q. Ouyang, V. Petrov, H. L. Swinney, *Phys. Rev. Lett.* **77**, 2105 (1996).
23. The control algorithm guides the wave along the target trajectory, generated by advancing the free parameter in Eq. 2. In the case where the trajectory intersects itself, we require the control algorithm to follow the advancing target trajectory.
24. F. Chirila, E. Mihaliuk, T. Sakurai, K. Showalter, in preparation.
25. A. Arkin, J. Ross, *J. Phys. Chem.* **99**, 970 (1995).
26. E. Mihaliuk, H. Skødt, F. Hynne, P. G. Sørensen, K. Showalter, *J. Phys. Chem. A* **103**, 8246 (1999).
27. M. Eigen, L. De Mayer, in *Technique of Organic Chemistry*, S. L. Friess, E. S. Lewis, A. Weissberger, Eds. (Interscience, New York, 1963), vol. 8 (no. 2), p. 895.

28. Supported by NSF grant number CHE-9974336 and the Office of Naval Research (grant number N00014-01-1-0596). K.S. thanks Alexander Mikhailov for his hospitality at the Fritz-Haber-Institut der Max-Planck-Gesellschaft and for many useful discussions that benefitted this study.

25 February 2002; accepted 18 April 2002
Published online 2 May 2002;
10.1126/science.1071265
Include this information when citing this paper.

A Reversible Solid-State Crystalline Transformation in a Metal Phosphide Induced by Redox Chemistry

D. C. S. Souza,[1] V. Pralong,[1] A. J. Jacobson,[2] L. F. Nazar[1]*

We demonstrate low-potential intercalation of lithium in a solid-state metal phosphide. A topotactic first-order transition between different but related crystal structures at room temperature takes place by an electrochemical redox process: $MnP_4 \leftrightarrow Li_7MnP_4$. The P–P bonds in the MnP_4 structure are cleaved at the time of Li insertion (reduction) to produce crystalline Li_7MnP_4 and are reformed after reoxidation to MnP_4, thereby acting as an electron storage reservoir. This is an unusual example of facile covalent bond breaking within the crystalline solid state that can be reversed by the input of electrochemical energy.

Crystalline transformations in the solid state are kinetically hindered reactions that typically occur on geological time scales without the benefit of high temperature, owing to the difficulty of transport within the bulk. An exception is intercalation, where ions are inserted and extracted within gaps in low-dimensional lattices with no substantial change to the lattice itself (*1*). These processes can take place at ambient conditions because of the minimal restructuring involved. They form the basis on which lithium-ion batteries function—namely, simultaneous reversible (de)intercalation of lithium ions at both high-potential (positive) and low-potential (negative) electrodes (*2*). Although all positive materials operate on this principle, graphitic carbon, used commercially, is the only material to display classical intercalation behavior at low potential (<1.0 V). $Li_4Ti_5O_{12}$ can intercalate one Li, but does so at a higher potential of 1.55 V (*3*). Other promising materials recently suggested for negative electrodes reversibly uptake lithium by other processes. These include alloying reactions in Li_xSn or Li_xSb nanophases (*4*, *5*), "uptake" by amorphous metal nitrides (*6*, *7*), and reduction to nanophasic metal or suboxide particles in metal oxides (*8*, *9*). Reaction of Li in the intermetallic phase Cu_6Sn_5 was reported to involve low-potential Li insertion involving Sn displacements within the lattice (*10*), although the breadth of the x-ray reflections made identification of the Li-rich phase ambiguous. Later evidence suggests that, during deep Li insertion, Sn is extruded from the lattice and Li-Sn alloying is responsible for Li uptake (*11*).

Here, we demonstrate low-potential intercalation behavior in a solid-state compound based on a metal phosphide. Phosphides lie between the more ionic nitrides and the intermetallic antimonides in their chemistry, but to date, little is known of their electrochemical behavior. We show that a topotactic first-order transition be

---

[1] Department of Chemistry and the Waterloo Centre for Materials Research, University of Waterloo, Waterloo, Ontario N2L 3G1, Canada. [2] Department of Chemistry, University of Houston, Houston, TX 77204, USA.

*To whom correspondence should be addressed. E-mail: lfnazar@uwaterloo.ca

tween different but related crystal structures at room temperature takes place: $MnP_4 \leftrightarrow Li_7MnP_4$ (*12*). The reversible interconversion of these crystalline phases is effected by an electrochemical redox process. The P–P bonds in the MnP_4 structure are cleaved on Li insertion (reduction), to give Li_7MnP_4, and are reformed on reoxidation to MnP_4, thereby acting as an electron storage reservoir.

The structure of MnP_4 is based on edge-sharing octahedra of MnP_6 that form infinite zigzag chains linked by covalent P–P bonds (Fig. 1A); it also can be viewed as a stacking of identical two-dimensionally infinite P nets (*13*). Numerous variants of this structure (n-MnP_4) exist that differ in the way these nets are stacked. In the case of 8-MnP_4, for example, eight layers are necessary to repeat the same stacking positions as the first layer. We focused on this variant because of its simple layered structure and good conductivity ($\sim 10^{-2}$ S/cm). Although this phase was originally prepared at a high pressure (*13*), we synthesized it by a tin-flux method. Ultrapure powders of manganese, red phosphorus, and tin were combined inside an argon-filled glove box (Mn:P:Sn equal to 1:10:6) and then transferred to a quartz tube that was evacuated and sealed. The tube was heated at 550 to 650°C for 2 weeks and quenched to room temperature. The resulting solid was treated with three portions of a 1:1 aqueous solution of HCl. The obtained shiny black crystals were stable in air, with particle sizes between 0.6 and 1.0 μm, and had an x-ray diffraction (XRD) pattern that matched that previously reported (*14*).

Reversible Li uptake of the materials was examined using lithium metal as both a pseudo-reference and counter-electrode in an electrochemical cell, as previously reported (*15*). The electrodes were dried for at least 4 hours before cell assembly, using a 1 M solution of $LiPF_6$ in 1:1 ethylene carbonate/dimethyl carbonate (EC/DMC). All the potential values are relative to the pair Li/Li^+. The voltage-composition curves for 6-MnP_4, on a discharge-charge-discharge cycle between 0.57 and 1.70 V at a rate of 1 Li/MnP_4 per 10 hours (C/10) (Fig. 1), exhibit a first-reduction (discharge) process characterized by a plateau at 0.62 V under these conditions. Slower rate studies show that the equilibrium potential (see below) is near 1 V. Regardless of the minimum imposed kinetics, reduction is complete at the end of the plateau with a capacity close to 7 Li.

The XRD reflections of the starting material MnP_4 (Fig. 2A) completely disappear on full discharge and are replaced by those of the well-crystallized antifluorite phase Li_7MnP_4. This change involves a substantial crystallographic modification. The antifluorite phase is usually described as close-packed layers of P arranged in a face-centered cubic (*fcc*) array, with Li and Mn atoms disordered on the tetrahedral sites (space group $Fm\bar{3}m$). A diagram of this structure depicting multiple-unit cells is displayed in Fig. 1B. Comparison with the very different zigzag layered structure of the starting phase MnP_4 (Fig. 1A) suggests that the solid-state conversion is not facile at room temperature.

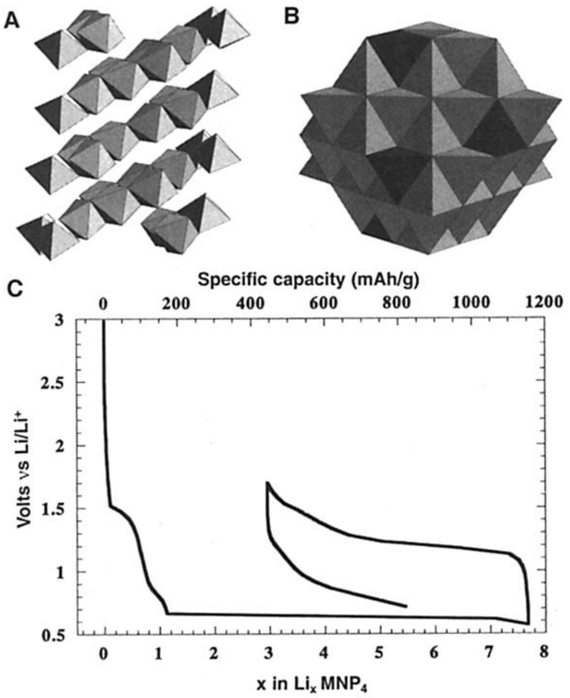

Fig. 1. (**A**) Structure of 8-MnP_4 in polyhedral motif showing the chains of MnP_6 octahedra linked by phosphorus atoms. (**B**) Structure of the antifluorite phase, Li_7MnP_4, illustrating edge-shared MnP_4 and LiP_4 tetrahedra. (**C**) Potential/composition curve on galvanostatic cycling of $MnP_4/Li^+/Li$ cells performed at a nominal C/10 rate (15 mA/g) in the 1.7 to 0.5 V potential window (mixed with 20 wt % carbon black and 5 wt % polyvinylidene difluoride).

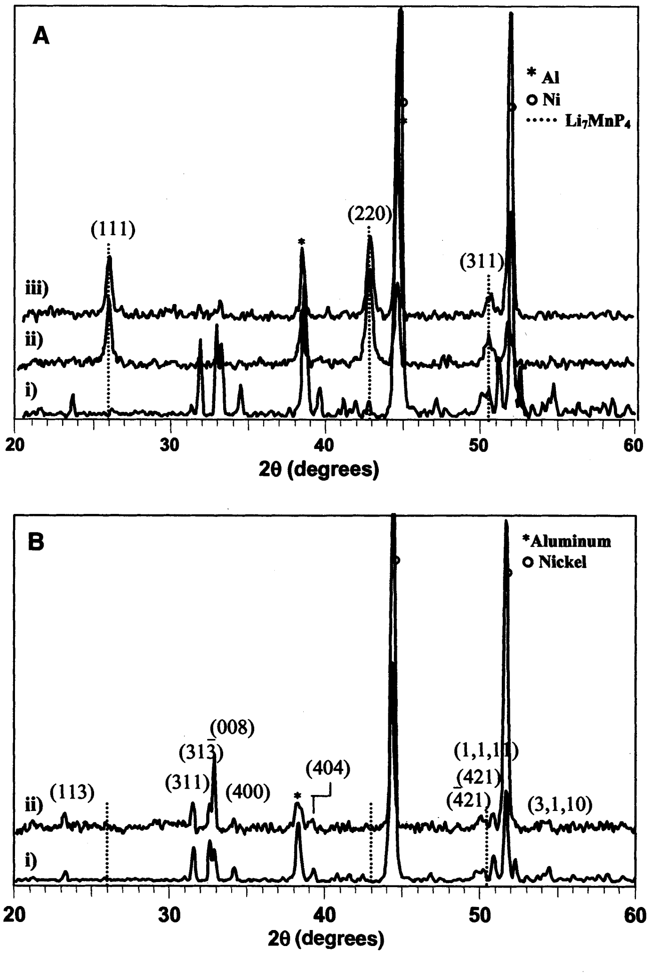

Fig. 2. Ex situ XRD patterns of MnP_4 at different cycling stages. (**A**) i, starting material 8-MnP_4; ii, at full discharge after one sweep; iii, after 10 cycles. (**B**) i, starting material; ii, at full charge (1.7 V) after five cycles. (A) and (B) were obtained on approximately 10 mg of sample, enclosed in a hermetically sealed holder. The indicated reflections from Al and Ni are contributions from the cell holder.

The structural transformation, surprisingly, can be reversed on reoxidation. On charge to 1.7 V, up to 5 Li/Mn are extracted, accompanied by electrochemical recrystallization of MnP_4, with no Li_7MnP_4 evident in the XRD pattern, even after five cycles (Fig. 2B). The loss in capacity arises from some irreversibility caused by loss of some material contact with the current collector, sluggishness of the transformation in the larger particles, and/or formation of amorphous material. The reversibility of the transformation on cycling is again evident in the XRD pattern on discharge, where Li_7MnP_4 is effectively the only material observable after 10 cycles to 0.6 V (Fig. 2A).

Scanning electron microscopy (SEM) images (Fig. 3) reveal morphological changes that accompany the structural transformation, which displays a change in texture and the appearance of cracks. Although the crystalline nature of the material is maintained throughout, there is a predictable reduction in particle size during this process owing to the substantial structural change between the two phases. The latter ultimately leads to a decrease in the reversible specific capacity during the first few cycles from 700 to 350 mAh/g, which stabilizes after 50 cycles (*16*). It is probable that a portion of the active material becomes dormant (electrochemically inaccessible) by lost of contact with the current collector, in accord with traces of MnP_4 being evident in the XRD pattern of the oxidized material after 10 cycles.

The reduction can also be achieved chemically, by treating MnP_4 with stoichiometric quantities of Li/NH_3, to yield crystalline Li_7MnP_4, as shown by XRD. The reverse process using chemical oxidation does not lead to a recognizable product. The kinetic and thermodynamic control accessible through electrochemical oxidation is clearly critical to nucleation of the recrystallized MnP_4 phase.

To confirm the true nature of the equilibrium ($MnP_4 + 7Li \leftrightarrow Li_7MnP_4$), galvanostatic intermittent titration (GITT) experiments were performed at a rate of C/50 to determine the equilibrium potential of the forward and back reaction (*17*). Interruptions of the current for periods greater than 10 hours were performed to obtain voltage drops smaller than 1 mV per hour (e.g., to reach approximately open circuit potential values). The fact that the equilibrium potential found for discharge (1.03 V) and charge (1.06 V) does not differ significantly indicates that the same reaction is involved in reduction and oxidation (despite the difference of the appearance in the plateau region). This emphasizes the reversibility of the process involved during insertion.

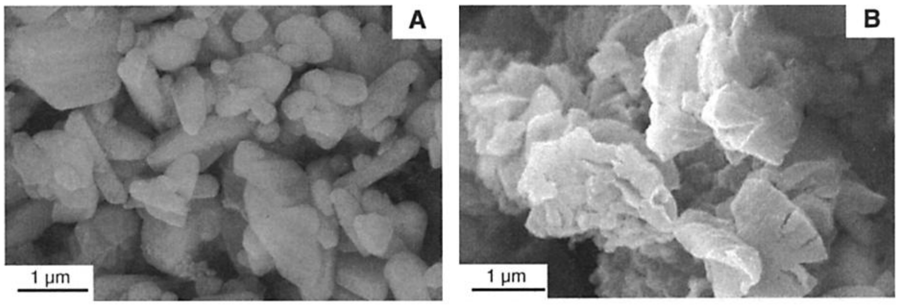

Fig. 3. SEM micrographs of the starting material MnP_4 (**A**) and fully discharged Li_7MnP_4 (**B**). The images were obtained using a LEO Gemini 1530 Field Emission SEM (LEO Electron Microscopy) with a resolution of 1 nm.

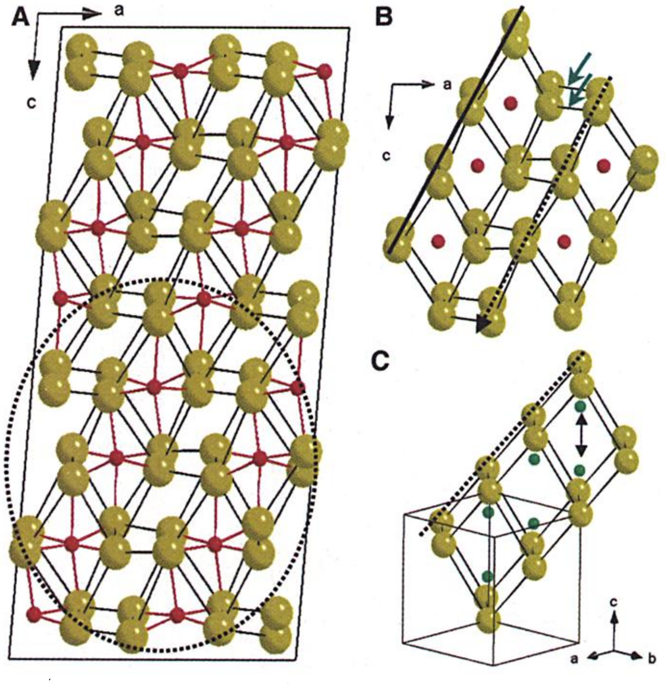

Fig. 4. Diagram showing the relation of the layered structure of MnP_4 to the antifluorite structure of Li_7MnP_4 and the proposed mechanism for the transformation. (**A**) Structure of 8-MnP_4 showing the octahedral coordination of the red Mn atoms within the rhomboids. (**B**) An excised portion of the MnP_4 structure indicated by the black circle in (A); the blue arrows indicate the P–P bonds that join the empty layers that are cleaved on Li insertion, and the dotted arrow depicts an example of the translation of P atoms that accompanies the bond cleavage. (**C**) The structure of Li_7MnP_4 in the same orientation shown in (B), with the blue atoms indicating either Mn or Li in tetrahedral coordination. The lines in the diagrams indicate the close-packed plane of P atoms that are in common in the two structures.

The structural transformations observed in this transition metal phosphide upon Li uptake/extraction suggest that facile bond cleavage and reformation is a signature of these highly covalent materials. Atom migration must be relatively rapid, because the conversion is evident at relatively high rates of up to 2C (discharge/charge in 0.5 hours). The fact that electrochemical recrystallization in the bulk solid at room temperature can occur at all, however, must be a consequence of similarity in phosphorus packing in the two structures. The relation between the two structures is illustrated in Fig. 4, along with a proposed mechanism for the transformation. The *fcc* structure of Li_7MnP_4 is shown in an alternate view in Fig. 4C, with the close-packed P layers indicated by a dotted line. The two tetrahedral sites contained within the phosphorus rhombohedra are randomly occupied by Li or Mn. In MnP_4, as shown in Fig. 4A, the P atoms within the chains of the Mn-P octahedra form slightly kinked close-packed layers. An alternative view of a small portion of this structure is shown in Fig. 4B, illustrating the similarity to the Li_7MnP_4 structure. We suggest that the initial reduction of MnP_4 induces cleavage of the P–P bonds that span the empty gaps (indicated by the arrows) and insertion of Li into the now-available sites. Translation of the P atoms forms undistorted cubic close-packed phosphorus layers. Accompanying this is a shift of the Mn within the rhomboids from octahedral to tetrahedral sites (Fig. 4C) to accommodate additional Li in the neighboring tetrahedral site. Hence, the Li_7MnP_4 structure results. On oxidation (Li extraction), the reverse process regenerates the crystalline MnP_4 layered structure.

These results are of interest both fundamentally and also with respect to possible applications. It is important that reduction, which accompanies the insertion of Li^+, must take place at the P–P centers (*18*). Unlike in most other intercalation compounds that accommodate guest species by redox chemistry that occurs at the metal cations, in metal phosphides it is primarily the anion that undergoes the redox reaction. The ensuing cleavage of the covalent P–P bonds is undoubtedly a consequence of the strong anion character of the uppermost lying electronic band. In this respect, phosphides have advantages over nitrides, such as isostructural Li_7MnN_4 (*19*), and the layered compounds $Li_{2.6-x}Co_{0.4}N$ (*6*, *7*) and $Li_{2.7}Fe_{0.3}N$ (*20*), proposed as negative electrodes. Differences in the strength of the M-pnictogen (P_N) bond and the relative contribution of the P_N–P_N bond result in a paucity of transition metal–poor binary nitrides; for example, MnN_4, analogous to MnP_4, does not exist. Because no binarynitrides are known that can reversibly uptake Li^+/e^-, the ternary nitrides must first be "charged" by electrochemical oxidation of Li from the structure, a drawback of these materials that also results in collapse to an amorphous structure. More importantly, the negative electrode in a cell should act as a reservoir for Li, as MnP_4 does, not a source.

In conclusion, the behavior of the phosphides represents a departure from that exhibited by ionic negative electrode materials, such as oxides (where the high energy of the metal-localized bands drives the reduction to the metallic state on Li uptake); nitrides; and intermetallic negative-electrode materials, where Li uptake relies on the formation of alloys Li_xM (M = Sb or Sn). Furthermore, facile covalent-bond rearrangement and atom migration that lead to electrochemical "recrystallization" are a signature of phosphides. New opportunities afforded by these materials will be explored in our forthcoming work (*21*), including iron and cobalt phosphides, where control of microstructure will be investigated as a route to facilitate structural conversion.

References and Notes

1. M. S. Whittingham, A. J. Jacobson, *Intercalation Chemistry* (Academic Press, New York, 1982).
2. M. Winter, J. O. Besenhard, M. E. Spahr, P. Novak, *Adv. Mater.* **10**, 725 (1998).
3. T. Ohzuku, A. Ueda, N. Yamomoto, *J. Electrochem. Soc.* **142**, 1431 (1995).
4. B. A. Boukamp, G. C. Lesh, R. A. Huggins, *J. Electrochem. Soc.* **128**, 725 (1981).
5. I. A. Courtney, J. R. Dahn, *J. Electrochem. Soc.* **144**, 2045 (1997).
6. T. Shodai, Y. Sakurai, T. Suzuki, *Solid State Ionics* **122**, 85 (1999).
7. Y. Takeda *et al.*, *Solid State Ionics* **130**, 61 (2000).
8. P. Poizot, S. Laruelle, S. Grugeon, L. Dupont, J.-M. Tarascon, *Nature* **407**, 499 (2000).
9. M. N. Obrovac, R. A. Dunlap, R. J. Sanderson, J. R. Dahn, *J. Electrochem. Soc.* **148**, A576 (2001).
10. K. D. Kepler, J. T. Vaughey, M. M. Thackeray, *Electrochem. Solid-State Lett.* **2**, 307 (1999).
11. G. X. Wang, L. Sun, D. H. Bradhurst, S. X. Dou, H. K. Liu, *J. Alloys Compounds* **299**, L12 (2000).
12. We use the term "topotactic" to imply a definite relation between crystallographic directions in the reactant and the product; the precise transformation mechanism is currently under investigation.
13. W. Jeitscko, P. C. Donahue, *Acta Crystallogr. B* **31**, 574 (1975).
14. Forty-three reflections observed out of a total of 43 (relative intensity >1) listed in the Joint Committee on Powder Diffraction Studies #30-0822; refined lattice parameters (LeBail method): a = 10.513 Å; b = 5.096 Å; c = 21.81 Å; β = 94.68°.
15. T. Kerr, J. Gaubicher, L. F. Nazar, *Electrochem. Solid-State Lett.* **3**, 460 (2000).
16. The contribution from lithium insertion into the carbon used as the additive in the electrode preparation is excluded from this value.
17. W. Weppner, R. A. Huggins, *J. Electrochem. Soc.* **124**, 1569 (1977).
18. Cleavage of anion-anion bonds along with reduction of the cation has been observed in the insertion of Li into TiS_3 [e.g., D. W. Murphy, F. A. Trumbore, *J. Electrochem. Soc.* **123**, 960 (1976)].
19. S. Suzuki, T. Shodai, *Solid State Ionics* **116**, 1 (1999).
20. J. L. C. Rowsell, V. Pralong, L. F. Nazar, *J. Am. Chem. Soc.* **123**, 8598 (2001).
21. V. Pralong, D. C. S. Souza, K. T. Leoung, L. F. Nazar, *Electrochem. Commun.* **4**, 516 (2002).

22. L.F.N. gratefully acknowledges the Natural Sciences and Engineering Research Council of Canada for funding this work, D.C.S. thanks CAPES/Brazil for financial support.

20 February 2002; accepted 19 April 2002

Co-Seismic Strike-Slip and Rupture Length Produced by the 2001 M_s 8.1 Central Kunlun Earthquake

Aiming Lin,[1]* Bihong Fu,[1] Jianming Guo,[2] Qingli Zeng,[3] Guangming Dang,[4] Wengui He,[5] Yue Zhao[3]

Field investigations show that the surface wave magnitude (M_s) 8.1 Central Kunlun earthquake (Tibetan plateau) of 14 November 2001 produced a nearly 400-kilometer-long surface rupture zone, with as much as 16.3 meters of left-lateral strike-slip along the active Kunlun fault in northern Tibet. The rupture length and maximum displacement are the largest among the co-seismic surface rupture zones reported on so far. The strike-slip motion and the large rupture length generated by the earthquake indicate that the Kunlun fault partitions its deformation into an eastward extrusion of Tibet to accommodate the continuing penetration of the Indian plate into the Eurasian plate.

Strike-slip faults often play an important role in horizontal extrusions of the lithosphere away from continental collision zones (*1*). The Tibetan plateau is a unique natural laboratory for studying collisional strike-slip faulting processes. There numerous tectonic blocks, some hundreds of kilometers wide, are moving eastward and southeastward along some major strike-slip faults to accommodate the ongoing northward penetration of the Indian plate into the Eurasian plate (*2*–*5*). The eastward extrusion of Tibet has generated 11 great earthquakes (with magnitudes between 7.5 and 8.7) in the past 300 years along the major strike-slip faults that bound the north side of Tibet (*6*). The 1200-km-long Kunlun fault striking E-W to WNW-ESE is one of the major collisional strike-slip faults in the Tibetan plateau (Fig. 1).

The M_s 8.1 Central Kunlun earthquake occurred on 14 November 2001 in the Kunlun mountain area (Fig. 1) (*7*). There were no reports of casualties or major damage, because the earthquake was centered in a remote area that is relatively flat, with elevation ranging between 4500 and 6860 m along the Kunlun fault. The motion on the fault due to the earthquake could not be determined from the seismic data (*8*–*11*) [Fig. 1 and table S1 (*12*)]. To determine the motion of the fault at the surface, the co-seismic displacement, and the rupture length, our survey group went to the epicentral area 5 days after the event.

The field investigations show that a nearly 400-km-long co-seismic surface rupture zone, called the Kunlun rupture zone hereafter, occurred mostly along the western (Kusai Lake) segment of the Kunlun fault (Fig. 1). The Kunlun fault cuts the south-sloping alluvial fans and bajada in the study area, which is recognized as a straight lineament trending E-W to WNW-ESE in the satellite images that were used for field mapping (Fig. 1). The surface ruptures were concentrated in a zone with a width ranging from 3 to 550 m, with an average width of 5 to 50 m. The zone is composed of distinct shear faults, extensional cracks, and mole tracks [Fig. 2 and figs. S1 and S2 (*12*)], mostly along the fault lineament shown in the satellite image (Fig. 1). The distinct shear fault planes were observed at sites 3 to 8, which strike N75°W to E-W, dip 75° to 90°N, and are parallel to the general trend of the surface rupture zone [Fig. 2B and fig. S1C (*12*)]. Horizontal slickenside striations were observed on the shear fault planes, which are marked by parallel lineations with some grooves and steps in the frozen allu-

---

[1] Institute of Geosciences, Faculty of Science, Shizuoka University, 836 Ohya, Shizuoka 422-8529, Japan. [2] Lanzhou Institute of Geology, Chinese Academy of Sciences, Lanzhou 730000, China. [3] Institute of Geomechanics, Chinese Academy of Geological Sciences, Beijing 100081, China. [4] Seismological Bureau of Qinghai Province, Xining, China. [5] Seismological Institute of Lanzhou, Lanzhou 730000, China.

*To whom correspondence should be addressed. E-mail: slin@ipc.shizuoka.ac.jp